Dynamics of the Reactions of $C(^3P_J)$ Atoms with Ethylene, Allene, and Methylacetylene at Low Energy Revealed by Doppler−Fizeau Spectroscopy†

Christian Naulin,*,‡,§ Nicolas Daugey,‡,§ Kevin M. Hickson,‡,§ and Michel Costes‡,§

Université de Bordeaux and CNRS UMR 5255, Institut des Sciences Moléculaires, 33405 Talence Cedex, France

Received: April 27, 2009; Revised Manuscript Received: July 29, 2009

The dynamics of the H-atom elimination reactions of $C(^3P_J)$ atoms with ethylene, allene, and methylacetylene have been investigated in experiments conducted with pulsed supersonic beams using a variable beam crossing angle configuration at relative translational energies, E_T, in the range of 0.7 to 5.5 kJ mol^{-1}. $H(^2S_{1/2})$ atoms were detected by time-of-flight mass spectrometry after sequential excitation to the $^2P°_J$ state using a laser beam tuned to the Lyman-α transition around 121.57 nm and ionization by a second laser beam at 364.7 nm. Doppler−Fizeau spectra of the recoiling H atoms were recorded in two configurations, with the Lyman-α laser beam oriented either parallel or perpendicular to the relative velocity vector of the reagents. A mathematical model developed to account for the density-to-flux transformation and to extract angular and recoil energy distribution functions from the experimental spectra by a forward convolution procedure is fully described. The model, applied to the C + C_2H_4 reaction, gives an excellent agreement with differential cross sections already determined in a previous combined study, thus providing a good test for its validity. All three processes are seen to pass through single pathways, identified by the comparison of the recoil energy distribution functions with the calculated reaction enthalpies, yielding H_2CCCH + H (for the C + ethylene reaction) and H_2CCCCH + H (for the C + allene and methylacetylene reactions). These results are discussed in the context of earlier experimental measurements performed at much higher collision energies.

1. Introduction

Doppler, or more precisely Doppler−Fizeau spectroscopy, is a useful method for determining beam velocities by using state-selective detection of quantum states.[1] The method also allows the determination of state-to-state (STS) differential cross sections (DCSs) $I(\theta,w')$ for products recoiling in the center-of-mass (CM) system with a velocity vector of w' modulus and θ scattering angle in crossed molecular beam (CMB) experiments. Measurements are generally conducted using two configurations with the excitation laser beam parallel or perpendicular to the relative velocity vector of the reagents. The parallel configuration, which directly yields the desired information in the CM system but which suffers from poor resolution near $\theta = 0$ and 180°, is indeed nicely complemented by the perpendicular configuration for better resolution at these latter scattering angles. Therefore, STS DCSs were obtained by Doppler−Fizeau spectroscopy for the first time in a study of the H + $NO_2 \rightarrow OH(v' = 0, J')$ + NO reaction[2] using laser-induced fluorescence (LIF) detection of the OH product and then for F + $I_2 \rightarrow IF(v', J')$ + F[3] and Cs(7p) + $H_2 \rightarrow CsH(v' = 0, J')$ + H[4] with LIF detection of IF and CsH, respectively. Later, two-color resonance-enhanced multiphoton ionization (1 + 1′ REMPI) coupled to time-of-flight mass spectrometric (TOF MS) detection of D atoms was used to extract DCSs for the CN + $D_2 \rightarrow$ DCN + D reaction.[5]

Although the Rydberg tagging[6] and Doppler-selected time-of-flight[5] techniques have become the preferred methods in recent years for obtaining DCSs when detecting recoiling H or D atoms from H/D-elimination reactions, Doppler−Fizeau spectroscopy remains a valuable method for gaining insight into the dynamics of reactions such as those of $C(^3P_J)$ with alkynes and alkenes: C + $C_nH_{2n} \rightarrow C_{n+1}H_{2n-1}$ + H and C + $C_nH_{2n-2} \rightarrow C_{n+1}H_{2n-3}$ + H. Indeed, Rydberg tagging and, to a lesser extent, Doppler-selected time-of-flight methods require saturation of the $(^2S_{1/2} \rightarrow {}^2P°_J)$ resonant step to fully or partially cover the Doppler profile, but the use of high photon fluxes at the Lyman-α wavelength, which does not generate signal-to-noise problems when reactions like F + $H_2 \rightarrow$ FH + H,[7,8] Cl + $H_2 \rightarrow$ HCl + H,[9,10] or $O(^1D_2)$ + $H_2 \rightarrow$ OH + H[11,12] are considered, is likely to produce a large background signal for reactions involving alkynes and alkenes because of significant photofragmentation of the hydrocarbon beam. For such reactions, operation in the linear absorption regime of the Lyman-α transition is preferable, a regime that precisely coincides with the application of Doppler−Fizeau (DF) spectroscopy. In this article, we demonstrate the usefulness of the method with an experimental arrangement first applied to the $C(^3P_J)$ + $C_2H_2 \rightarrow C_3H$ + H reaction,[13] making use of two orthogonal laser beams steered at the collision center, the first one exciting the $(^2S_{1/2} \rightarrow {}^2P_J)$ transition in a linear regime, the second one realizing the ionization step in a highly saturated regime but without added background interference. We develop a full model accounting for the density-to-flux transformation to retrieve DCSs by a forward convolution procedure. Finally, we examine the DCSs derived using this model from the DF spectra obtained for the $C(^3P_J)$ + $C_2H_4 \rightarrow C_3H_3$ + H and $C(^3P_J)$ + C_3H_4 (methylacetylene and allene) $\rightarrow C_4H_3$ + H reactions. These C−H insertion−elimination reactions are of potential astrophysical interest for the chemistry of dense interstellar clouds ($T \approx 10-50$ K): (i) they result in the synthesis of larger unsaturated carbon-bearing species, and (ii) they do not exhibit

† Part of the "Vincenzo Aquilanti Festschrift".

* Corresponding author. E-mail: c.naulin@ism.u-bordeaux1.fr. Tel: +33-5-40 00 24 67. Fax: +33-5-40 00 66 45.

‡ Université de Bordeaux.

§ CNRS UMR 5255.

10.1021/jp9038545
Published on Web 08/27/2009

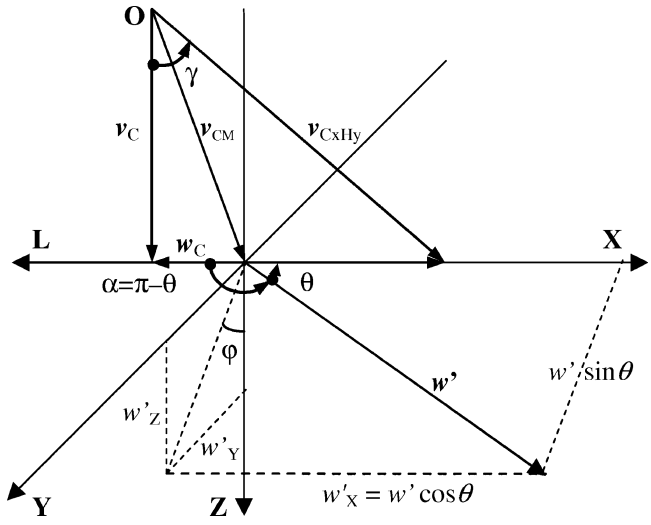

Figure 1. Schematic Newton view in the parallel configuration. {*X*, *Y*, *Z*}: center-of-mass frame, {CM}, attached to the center-of-mass (CM) and translating at a velocity v_{CM} relative to the laboratory frame, {LAB} (not shown for clarity). **L**: laser propagation axis (antiparallel to *X* axis). Angles: θ and φ refer to recoil CM-velocity angles of the atomic (H) detected fragment; θ is defined with respect to molecular coreactant (C_2H_4) so that $\theta = 0$ corresponds to forward scattering (C_3H recoils in the C-beam direction, whereas H recoils in the C_2H_4-beam direction); γ is the beam intersection angle; α is the angle between $\boldsymbol{w'}$ and **L**. In this configuration, reagent velocities are selected so that $\boldsymbol{v'}_r \perp \boldsymbol{v}_C$.

any significant energy barrier, as shown by kinetics as well as dynamics measurements.[14−16] This indeed is of crucial importance at the low temperatures prevailing in these media.

2. Experimental Section

Experiments were performed with an all pulsed and variable beam intersection angle CMB machine, the main features of which have been previously described.[17] In brief, the atom beam was produced by ablating C atoms from a graphite rod in slow helical motion. A fraction of the output, ca. 0.2 mJ, from a quadrupled Nd/YAG laser (Spectra-Physics LAB 150, 10 Hz, 8 ns, 60 mJ at 266 nm) was focused to a 0.05 mm waist on the graphite rod, and the ablated atoms were subsequently entrained into the supersonic expansion of Ne carrier gas emitted by a first fast-pulsed valve operating at 10 Hz (Beam Dynamics).[18] This skimmed, pulsed $C(^3P_J)$ beam of velocity v_C was collided at a given intersection angle in the range $22.5 \leq \gamma \leq 60°$ with a skimmed, pulsed C_xH_y coreactant beam of velocity $v_{C_xH_y}$ produced by a second fast-pulsed valve operating at 5 Hz (Beam Dynamics). The background pressure remained $<10^{-4}$ Pa with both beams in operation, and the attenuation of one beam by the other one was <4%. Experiments were performed at selected relative translational energies between $E_T \approx 0.7$ and 5.5 kJ mol^{-1} under beam conditions satisfying the relationship $v_C = v_{C_xH_y} \cos\gamma$, hence providing a relative velocity vector of reagents, v_r, perpendicular to the C beam and along the axis of one the laser beams. (See Figure 1.) The relevant beam conditions are summarized in Table 1.

$H(^2S_{1/2})$ atoms produced by the reaction were detected by resonance-enhanced two-color ionization with sequential absorption of a photon in the vacuum UV (VUV) tuned to the Lyman-α ($^2S_{1/2} \rightarrow {}^2P°_J$) transition at 121.57 nm and a UV photon at 364.7 nm for threshold ionization. The laser system consisted of a Nd/YAG laser locked to a single longitudinal mode (Spectra-Physics PRO 230, 10 Hz, 10 ns, 1.3 J @ 1064 nm and 0.003 cm^{-1}) and a dye laser (Quantel TDL50, 0.05 cm^{-1}) pumped by the Nd/YAG second harmonic at 532 nm. A UV beam (ca. 24 mJ, 8 ns) at 364.7 nm was obtained by sum-frequency mixing tunable 554 nm radiation from the dye laser with residual 1064 nm radiation in a beta barium borate (BBO) crystal (Inrad AT3-UV, BBO 36° cut) and was separated into two components with a beam splitter. In the configuration henceforth referred to as parallel, the first beam with ca. 7 mJ energy propagated in the molecular beam scattering plane parallel to v_r and was focused with a movable lens ($f = 92$ mm at 364.7 nm) into a cell filled with ca. 12 kPa of Kr set at the entrance of a light baffle arm 1 m away from the collision center. The tunable VUV radiation produced by frequency tripling was collimated by a fixed MgF_2 lens ($f = 130$ mm at 120 nm) that also acted as the exit window of the cell. The large difference in refractive index of MgF_2 between the VUV and the UV eliminated most of the divergent incident UV radiation before reaching the scattering center. The intensity of the VUV beam pulses was monitored by a fast-time-response detector with a Ni photoemissive cathode[19] mounted on the exit light baffle arm, the output of which was fed into a first boxcar integrator (Stanford Research Systems SR250). The second beam with ca. 17 mJ energy was steered at the collision center perpendicular to the first one and the scattering plane along the main axis of the collision chamber. In the configuration henceforth referred to as perpendicular, the beam paths of the VUV and UV lasers were interchanged. Both laser beams crossed between specially cut acceleration plates, which allowed the molecular beams to pass through, of a linear two-stage Wiley−MacLaren[20]

TABLE 1: Characteristics of the Pulsed Supersonic Beams

gas mixture	P (MPa)[a]	V (m s^{-1})[b]	$\Delta v/v$[c]	Δt (μs)[d]	γ (deg)[e]	E_T (kJ mol^{-1})[f]
C-atom beam						
Ne	0.7	1000 ± 4	0.17 (0.07)[g]	25	0	
Ethylene Beam						
C_2H_4:0.45/He:0.55	0.17	1111 ± 5	<0.15	32	22.5	0.76⊥
C_2H_4:0.10/He:0.90	0.25	1543 ± 5	<0.10	25	47.8	5.5 ⊥
id.					49.1	5.7 //
C_2H_4:0.50/He:0.50	0.16	1080 ±5	<0.15	32	22.5	0.72//
Allene Beam						
H_2CCCH_2:0.32/He:0.68	0.18	1115 ± 5	<0.15	32	22.5	0.84⊥
id.					46.9	3.3 ⊥
id.					60	5.2 ⊥
H_2CCCH_2:0.36/He:0.64	0.18	1089 ± 5	<0.15	33	22.5	0.80//
H_2CCCH_2:0.15/He:0.85	0.24	1317 ± 5	<0.10	28	40.6	3.4 //
Methylacetylene Beam						
H_3CCCH:0.32/He:0.68	0.18	1115 ± 5	<0.15	32	22.5	0.84⊥
id.					46.9	3.3 ⊥
H_3CCCH:0.36/He:0.64	0.18	1084 ± 5	<0.15	33	22.5	0.80//
H_3CCCH:0.15/He:0.85	0.24	1317 ± 5	<0.10	28	40.6	3.4 //

[a] Backing pressure. [b] Velocity at the peak and statistical uncertainty at the 95% confidence level. C beam: from TOF between the ablation beam waist and C atoms detected in the crossing region, 140 mm downstream, by (2 + 1) REMPI on $2p^2\ ^3P_J \rightarrow 2p3p\ ^3P_J$ transitions near 280 nm. C_xH_y beam: TOF measurements with fast-ionization gauges (ref 18) inserted at nine positions between 85 and 285 mm from the nozzle. Systematic errors are estimated to be <4% for the C beam and <2% for the C_xH_y beam. [c] Velocity spread full width at half-maximum (fwhm). [d] Pulse width (fwhm) in the beam crossing region 140 mm from ablation point for the C beam and 110 mm from the nozzle for the C_xH_y beam. [e] Beam crossing angle. The beam divergence is estimated to be 4° fwhm for both beams. [f] Relative translation energy when crossed with the C/Ne beam in the perpendicular (⊥) or parallel (//) configuration. [g] Actual velocity spread for C atoms undergoing reactive collisions with the C_xH_y beam. Because the C-atom beam is fully dispersed in the beam-crossing region, atoms traveling in front of the pulse are the fastest and those at the end are the slowest.

TOF MS (Stefan Kaesdorf Gmbh) positioned in the beam scattering plane at 135° to the C-atom beam. The H^+ signal collected on the microchannel plates was gated by a second boxcar integrator (Stanford Research Systems SR250). The H^+ and VUV signals were acquired for each individual laser shot, allowing for subsequent normalization (I_{H+}/I_{VUV}) because the VUV absorption process was maintained in the linear regime whereas the UV ionization step was in the high-saturation regime under our operating conditions.

Two sources of background H atoms had to be treated in the present experiments: (i) a faint one due to hot H atoms resulting from the dissociation of the C_xH_y beam into $C_xH_{y-1} + H$ giving rise to a DF spectrum with a large energy spread, and (ii) a strong one due to cold H atoms originating from the ablation process and highly cooled within the supersonic expansion of the carrier gas, giving rise to a very narrow DF spectrum. By firing of the lasers and the carbon beam at 10 Hz and the C_xH_y beam at 5 Hz, both the total signal including the reactive signal with backgrounds i and ii and the signal from background ii alone were alternatively recorded. Background i was recorded in separate scans with the hydrocarbon beam alone under the same operating conditions. It was found to be negligible for ethylene and allene (no neat signal could be extracted from the noise) but not for methylacetylene: this contribution could be fitted as a simple Gaussian function and was added to the synthetic DF spectrum in the fitting procedure.

Experiments were conducted with 10 laser shots separately recorded at each fundamental wavelength of the dye laser incremented by 2.5 pm steps and lasted <450 s, thus avoiding any drift in the experimental conditions. The wavelength of the UV was tracked on a shot-to-shot basis with a wavemeter (Cluster LM-007, 10^{-7} resolution), and absolute calibration on each scan was given by background ii. Because the collimated atom beam was perpendicular to the Lyman-α laser, the projection of its velocity along the laser axis was zero, and hence the cold H atoms encountered no DF shift at all. In other words, background ii revealed λ_0 and the bandwidth of the VUV laser. Shot-to-shot acquisition rather than averaging several shots at each wavelength increment of the tunable laser led to a sharp laser line width ($\Delta\lambda/\lambda < 10^{-6}$), as can be seen on background ii, and allowed for complete separation of the two doublet peaks ($^2S_{1/2} \rightarrow {}^2P°_{3/2}$) and ($^2S_{1/2} \rightarrow {}^2P°_{1/2}$) of the Lyman-α transition. Indeed, each individual laser shot was assigned to its actual UV wavelength, thus avoiding any blurring effect due to instabilities in the oscillator of the dye laser, and shots showing too complex a multimode structure, ca. 30% of the shots were single longitudinal mode, were rejected by the wavemeter. Doppler−Fizeau spectra consisting of ca. 4000 reactive events were generated by averaging over six to seven experimental scans after subtraction of background ii from the total signal.

3. Data Analysis: Description of the Model

3.1. Principles. A species scattered with a velocity vector v' in the laboratory frame contributes to the signal observed at a given laser excitation wavelength, as expressed in the Doppler−Fizeau relationship: $\lambda_L = \lambda_0(1 - v_L'/c)$, where λ_0 represents the unshifted line center of the probed transition, v_L' represents the projection of v' on the laser propagation axis, and c represents the speed of light.

The signal intensity within a spectral element $d\lambda_L$ around λ_L is proportional to the number of species such that their velocity projection on the laser axis, v_L', is constant for any possible combination of v' values and orientation.

If the species probed is a product of reactive collisions, then this number depends on the production flux and hence on the DCS. It also depends on the density distributions (radial and temporal for pulsed beams) of the beams insofar as flux-to-density conversion must be achieved. A forward convolution procedure is used. The spectrum is calculated with a trial DCS (angular and velocity distribution functions) and compared with the experimental spectrum. The trial functions are adjusted to allow for the best fit.

The following sections describe: (i) the scattered flux in terms of the DCS and the modeling of the DCS with distribution functions and (ii) the computation of the Doppler−Fizeau spectra.

The flux-to-density conversion for a pulsed, CMB experiment (assuming Gaussian spatial and temporal distributions for both beams) is described in the Appendix.

3.2. Scattered Flux. In a typical crossed beam experiment, the flux of product measured in a small element of solid angle $\Delta\Omega_D$ seen by the detector with velocity resolution $\Delta v'$ in the laboratory frame {LAB} is

$$I(\Theta, v') = \frac{d^3\dot{N}}{d^2\omega\, dw'} J\Delta\Omega_D\Delta v' \quad (1)$$

where v' and w' stand for the velocity of the detected fragment in the {LAB} frame and in the CM frame, respectively, and $J = (d^2\omega\ dw')/(d^2\Omega\ dv') = v'^2/w'^2$ is the Jacobian of the transformation.

The total flux of production is $\dot{N} = n_1 n_2 \Delta V \sigma_R v_r$, where n_1 and n_2 are the number densities of the reagents, ΔV is the element of volume of interaction considered (in the crossing region of the beams), σ_R is the integral cross section (ICS) of reaction, and v_r is the relative velocity of the reagents. Deriving $\dot{N}$ with respect to ω and w' yields

$$\frac{d^3\dot{N}}{d^2\omega\, dw'} = n_1 n_2 \Delta V v_r \frac{d^3\sigma}{d^2\omega\, dw'} \quad (2)$$

where $d^3\sigma/(d^2\omega\ dw') = I(\theta,w')$ is the DCS.

In a classical crossed-beam experiment (i.e., mass spectrometric detection with velocity and angular resolution), one can thus determine the DCS if one knows the Jacobian, J

$$I(\Theta, v') = n_1 n_2 \Delta V v_r \frac{d^3\sigma}{d^2\omega\, dw'} J\Delta\Omega_D\Delta v' \quad (3)$$

The flux in the {LAB} frame, $I(\Theta,v')$, is generally reconstructed via a forward convolution process assuming that the θ and w' variables are separable, which makes it possible to write the DCS in the form

$$I(\theta, w') = C \times P(w') \times T(\theta) \quad (4)$$

where $P(w')$ and $T(\theta)$ stand for the velocity and angular distribution functions, respectively, and C is a normalization factor; $C = \sigma_R/2\pi$ when both functions are normalized to unity, that is

$$\int_0^\infty P(w')\, dw' = 1 \quad \text{and}$$
$$\int_0^\pi T(\theta) \sin\theta\, d\theta = \int_{-1}^{+1} T(\cos\theta)\, d\cos\theta = 1 \quad (5)$$

In the following, the DCSs will be defined according to eqs 4 and 5.

TABLE 2: Definition of Velocity Vectors in the Parallel Configuration[a]

	CM velocity: v_{CM}	product velocity in{CM}: w'	product velocity in {LAB}: $v' = v_{CM} + w'$
X	$v_X(CM) = w_C$	$w'_X = w' \cos\theta$	$v'_X = +w_C + w' \cos\theta$
Y	$v_Y(CM) = 0$	$w'_Y = w' \sin\theta \sin\varphi$	$v'_Y = 0 + w' \sin\theta \sin\varphi$
Z	$v_Z(CM) = v_C$	$w'_Z = w' \sin\theta \cos\varphi$	$v'_Z = v_C + w' \sin\theta \cos\varphi$

[a] v_C, w_C, v', and w' stand for the moduli of velocity vectors $\mathbf{v}_C$, $\mathbf{w}_C$, $\mathbf{v}'$, and $\mathbf{w}'$. Indeed, if the atom beam is not oriented along the Z direction, then the condition $\mathbf{L}//\mathbf{v}'_r$ no longer fullfills the condition that $\mathbf{v}'_r \perp \mathbf{v}_C$. In that case, $v_X(CM)$, $v_Y(CM)$, and $v_Z(CM)$ must be explicitly kept in the expression of the v' components.

Note that this assumption is not strictly necessary; it does, however, simplify calculations because it drastically reduces the number of parameters needed to describe the distributions. When it is not valid, other methods may be used to model DCSs, such as phase space theory, as shown by Bonnet et al.[21] for the reactions $O(^1D,^3P) + ICH_3$ and $C(^1D) + H_2$.

3.3. Modeling Angular and Velocity Distribution Functions. The DCS is usually expressed in terms of the recoil energy distribution of the products, $P(E'_T)$. If v'_r is the relative velocity of separation of the products, then $P(E'_T)\, dE'_T = P(v'_r)\, dv'_r$.

The distribution can be modeled with a simple function with three parameters

$$P(E'_T) = \left\{1 - \frac{E'_T}{E_{tot}}\right\}^m \left\{\frac{E'_T}{E_{tot}}\right\}^n \exp\left\{-p\frac{E'_T}{E_{tot}}\right\}$$

$$= \{1 - x^2\}^m x^{2n} e^{-px^2} \quad (6)$$

where E_{tot} is the total energy available for the products, $x = v'_r/v'_{max}$, and v'_{max} is the maximum v'_r value compatible with energy conservation; note that $x^2 = E'_T/E_{tot}$. The case $m = n = {}^1/_2$, $p = 0$ corresponds to an unconstrained statistical distribution, that is, the "prior" one in the sense of Levine and Bernstein.[22] Noting that $dE'_T = \mu' v'_r\, dv'_r = \mu' v'^2_{max} x\, dx$, where μ' is the reduced mass of recoiling products, it becomes (in reduced units): $P(x) = \mu' v'^2_{max}\{1 - x^2\}^m x^{2n+1} e^{-px^2}$ with indeed $P(x)\, dx = P(E'_T)\, dE'_T$.

The angular distribution function may be conveniently expressed as a projection on a basis of Legendre polynomials of the first kind

$$T(\theta) = \sum_l c_l P_l(\cos\theta) \quad (7)$$

3.4. Doppler−Fizeau Spectra. The calculation of Doppler−Fizeau spectra is performed by adapting the method originally developed by Serri et al.[2] to our experiment, in particular, by including the flux−density conversion. Details concerning the Doppler−Fizeau analysis can be found elsewhere.[2,4,5] Only the main features concerning our particular experiment are presented.

3.4.1. Parallel Configuration. The modulus of $\mathbf{v}'$ is

$$v' = \{w_{C^2} + v_{C^2} + w'^2 + 2w_C w' \cos\theta + 2v_C w' \sin\theta \cos\varphi\}^{1/2} \quad (8)$$

and its projection on the laser axis is $v_L' = -w_C + w' \cos\alpha$.[23] (See Figure 1 for the axes orientation convention and Table 2 for definitions of the vectors.)

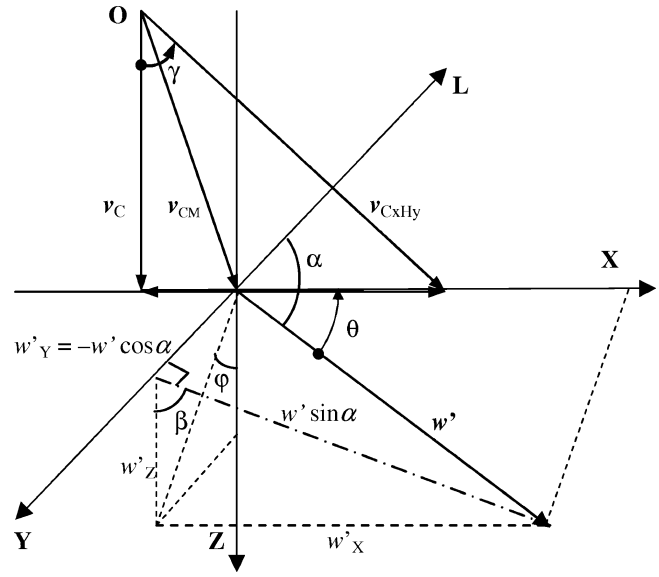

Figure 2. Schematic Newton view in the perpendicular configuration. Same symbols as in Figure 1. Note that α still refers to the angle between $\mathbf{w}'$ and $\mathbf{L}$; β refers to the position of the $\{\mathbf{Y},\mathbf{w}'\}$ plane around the laser axis.

As the VUV laser counterpropagates along the X axis, the angle α between the laser and the velocity (in the CM frame) of the product probed is: $\alpha = \pi - \theta$. The Doppler−Fizeau shift is thus

$$\lambda_L - \lambda_0 = -\lambda_0[v_L'/c] = +\lambda_0[w_C + w' \cos\theta]/c \quad (9)$$

Note that the CM motion results in a red shift of the whole line by $\lambda_0\, w_C/c$, whereas the relative motion in the CM frame results in a shift (broadening) of $\lambda_0\, w' \cos\theta/c$. The spectrum of H atoms forward scattered ($\theta < 90°$) will also be red-shifted.

The flux in the CM frame of H atoms recoiling with a definite velocity vector is

$$\frac{d^3\dot{N}}{d^2\omega\, dw'} = n_1 n_2 \Delta V v_r \frac{d^3\sigma}{d^2\omega\, dw'} \quad (10)$$

where the solid angle element is: $d^2\omega = \sin\theta\, d\varphi\, d\theta$. Assuming the DCS to be separable (eq 4) yields the following expression for the flux of production

$$\frac{d^3\dot{N}}{d^2\omega\, dw'} = n_1 n_2 \Delta V \frac{\sigma_R}{2\pi} v_r P(w') T(\theta) \quad (11)$$

We obtained the number of H atoms present in the detection volume when the probe laser is triggered (at $t = 0$) by integrating the flux on time (from $-\infty$ to 0) with the constraint that the product must lie in the probe volume at $t = 0$ to be detected. (See the Appendix for details.) Because the products are probed in the beam crossing region, they cannot be discriminated with respect to their recoil orientation. It is thus necessary to sum over all possible orientations giving the same velocity component along the laser axis. The signal intensity at a given excitation wavelength, λ, is proportional to the number of H atoms absorbing per spectral element

$$\left|\frac{d^2N}{d\lambda}\right| = n_1^0 n_2^0 \Delta V \sigma_R v_r \frac{c}{\lambda_0} \frac{P(w')}{w'} T(\theta)\, dw' \langle \Delta t \rangle_\varphi \qquad (12)$$

where the term $\Delta t(w', \theta, \varphi)$, deduced from integration, corresponds to the interaction time averaged over all possible φ values (cf. Appendix, eq A18).

The total signal is obtained when integrating numerically this equation on w' for each spectral element with the constraint that the spectral element concerned remains constant, which implies that the projection of $\boldsymbol{w}'$ on the laser axis, $u = w' \cos(\pi - \theta) = -w' \cos \theta$, remains constant.

The spectrum can then be computed for trial distribution functions

$$I(\lambda) \propto K \sum_i \langle \Delta t_i \rangle_\varphi P(w'_i) T(\theta_i) \delta w' / (w'_i) \qquad (13)$$

where the term K includes all factors that remain constant for a given experiment

$$K = n_1^0 n_2^0 \Delta V \sigma_R v_r \frac{c}{\lambda_0} \qquad (14)$$

TABLE 3: Definition of Velocity Vectors in the Perpendicular Configuration

	CM velocity: $\boldsymbol{v}_{CM}$	product velocity in{CM}: $\boldsymbol{w}'$	product velocity in {LAB}: $\boldsymbol{v}' = \boldsymbol{v}_{CM} + \boldsymbol{w}'$
X	v_X(CM)	$w'_X = w' \sin\alpha \sin\beta$	$v'_X = v_X$(CM) + $w' \sin\alpha \sin\beta$
Y	v_Y(CM) = 0	$w'_Y = w' \cos(\pi - \alpha) = -w' \cos\alpha$	$v'_Y = 0 - w' \cos\alpha$
Z	v_Z(CM)	$w'_Z = w' \sin\alpha \cos\beta$	$v'_Z = v_Z$(CM) + $w' \sin\alpha \cos\beta$

Another experimental factor has to be taken into account. The microchannel plate detector of the TOF mass spectrometer is limited by a 20 mm diameter aperture. Ions with a velocity component perpendicular to the TOF MS axis higher than a maximum value, v_{max}, will drift during the time-of-flight ($t_f \approx 0.81\ \mu s$ for H^+) and fall outside of the aperture; such ions will not contribute to the signal. A procedure was added in the fitting program to disregard those undetected ions corresponding to a value $v_{max} = 12\,300\ ms^{-1}$.

The spectrum is finally convoluted with the apparatus function, which was determined in the experiment described above as the spectrum due to "cold" H atoms produced within the C-atom beam for which there is neither a DF shift (beam perpendicular to the laser axis) nor broadening (translational temperature <10 K).

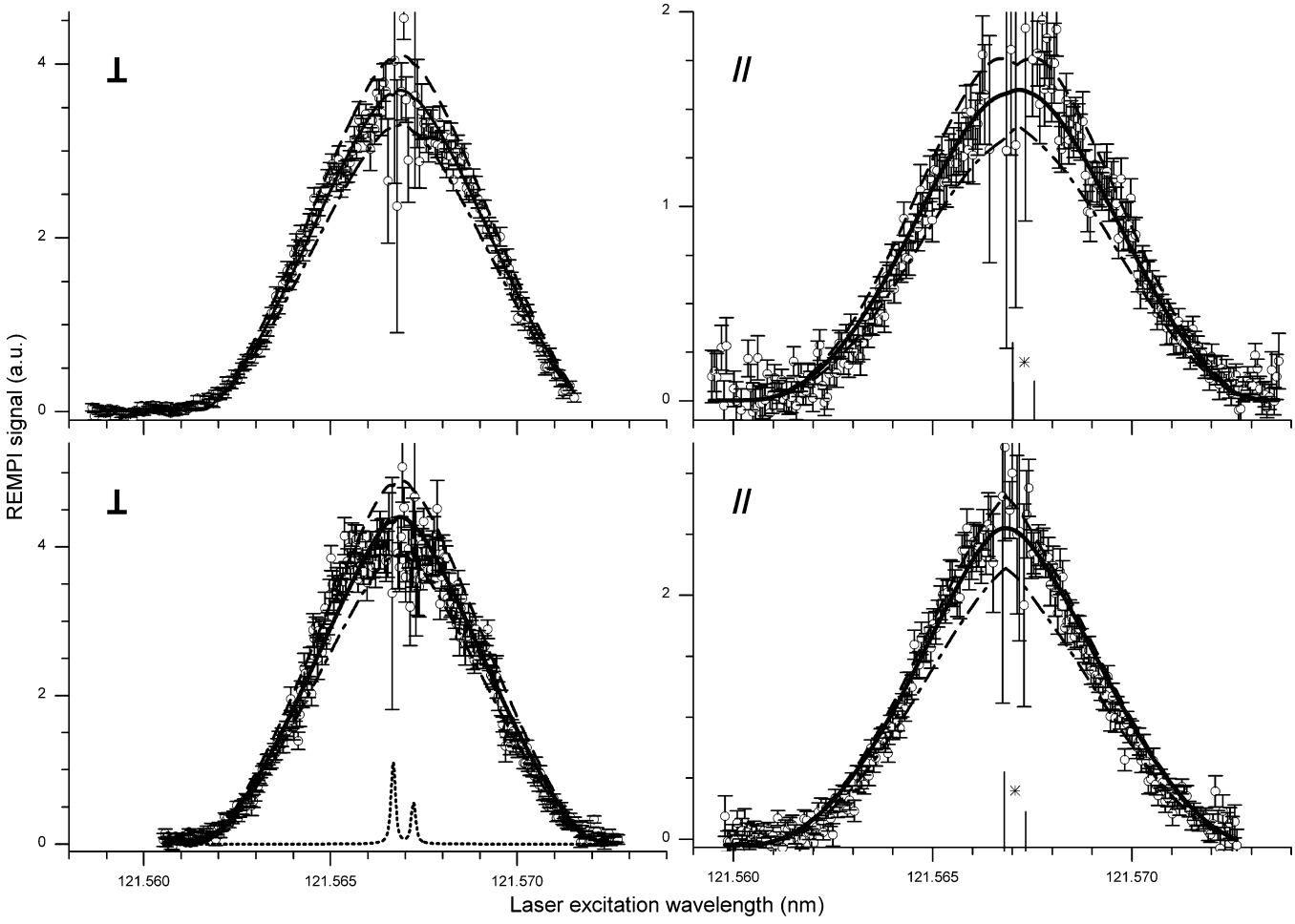

Figure 3. DF spectra of the H product from the C + C_2H_4 reaction at 0.7 kJ mol^{-1} (lower row) and 5.5 kJ mol^{-1} (upper row) in the perpendicular (⊥) and parallel (//) configurations. Experimental (○); Fitting functions: best fit (solid line); dashed and dashed-dotted lines limit the range of acceptable fits; apparatus function (dotted line). Lyman-α ($^2S_{1/2} \rightarrow {}^2P°_{3/2}$ and $^2S_{1/2} \rightarrow {}^2P°_{1/2}$) line positions in the CM frame are indicated (*). Intensities are given in arbitrary units (a.u.).

The obtained spectrum is then compared with the experimental spectrum. The procedure is repeated with new trial functions until a satisfactory fit is obtained. In fact, it should be noted that spectra obtained in both parallel and perpendicular configurations must be described with the same DCS functions: it is thus preferable to fit both spectra concurrently.

3.4.2. Perpendicular Configuration. In this configuration, the VUV laser counterpropagates along the ***Y*** axis. (See Figure 2 for the axes orientation convention and Table 3 for definitions of the vectors.) The modulus of $\boldsymbol{v}'$ now reads

$$v'_{\mathrm{H}} = \{v_X(\mathrm{G})^2 + v_Z(\mathrm{G})^2 + w'^2 + 2w'\sin\alpha\,[v_X(\mathrm{G})\sin\beta + v_Z(\mathrm{G})\cos\beta]\}^{1/2} \quad (15)$$

The Doppler−Fizeau shift is now given by

$$\lambda_{\mathrm{L}} - \lambda_0 = -\lambda_0 w'\cos\alpha/c \quad (16)$$

There is no contribution due to the CM motion because in this configuration, the laser is perpendicular to $\boldsymbol{v}_{\mathrm{CM}}$. Furthermore, the shift will be symmetrical with respect to $\alpha = \pi/2$ because [**X**,**Z**] is a plane of symmetry of the system. The line will be centered at λ_0.

The flux of production and the number of H atoms recoiling with a definite velocity vector are indeed the same as those in the parallel configuration. The corresponding contribution to the spectrum is

$$\left|\frac{\mathrm{d}^3N}{\mathrm{d}\lambda}\right| = KP(w')\frac{\mathrm{d}w'}{w'}\frac{1}{4\sqrt{\pi}}\frac{T(\theta[\alpha,\beta])\,\mathrm{d}\beta}{\sqrt{\alpha_1^2+\alpha_2^2}} \quad (17)$$

where K is the constant defined in eq 14 and α_i is defined in the Appendix (eqs A8 and A12). The total signal at a given λ is computed numerically by summing eq 17 over all possible values of β and α and then w', with the constraint that u = constant, which implies that for each w'_j value, $\cos\alpha_j = -u/w'_j$

$$I(\lambda) \propto K\sum_j \langle\Delta t(\alpha_j)\rangle_\beta P(w'_j)\delta w'/(w'_j) \quad (18)$$

where $\langle\Delta t(\alpha_j)\rangle_\beta$ now represents the interaction time averaged over all possible β values for a given value of the α_j angle (cf. Appendix, eq A19).

As in the former case, the spectrum is obtained by convolution with the apparatus function.

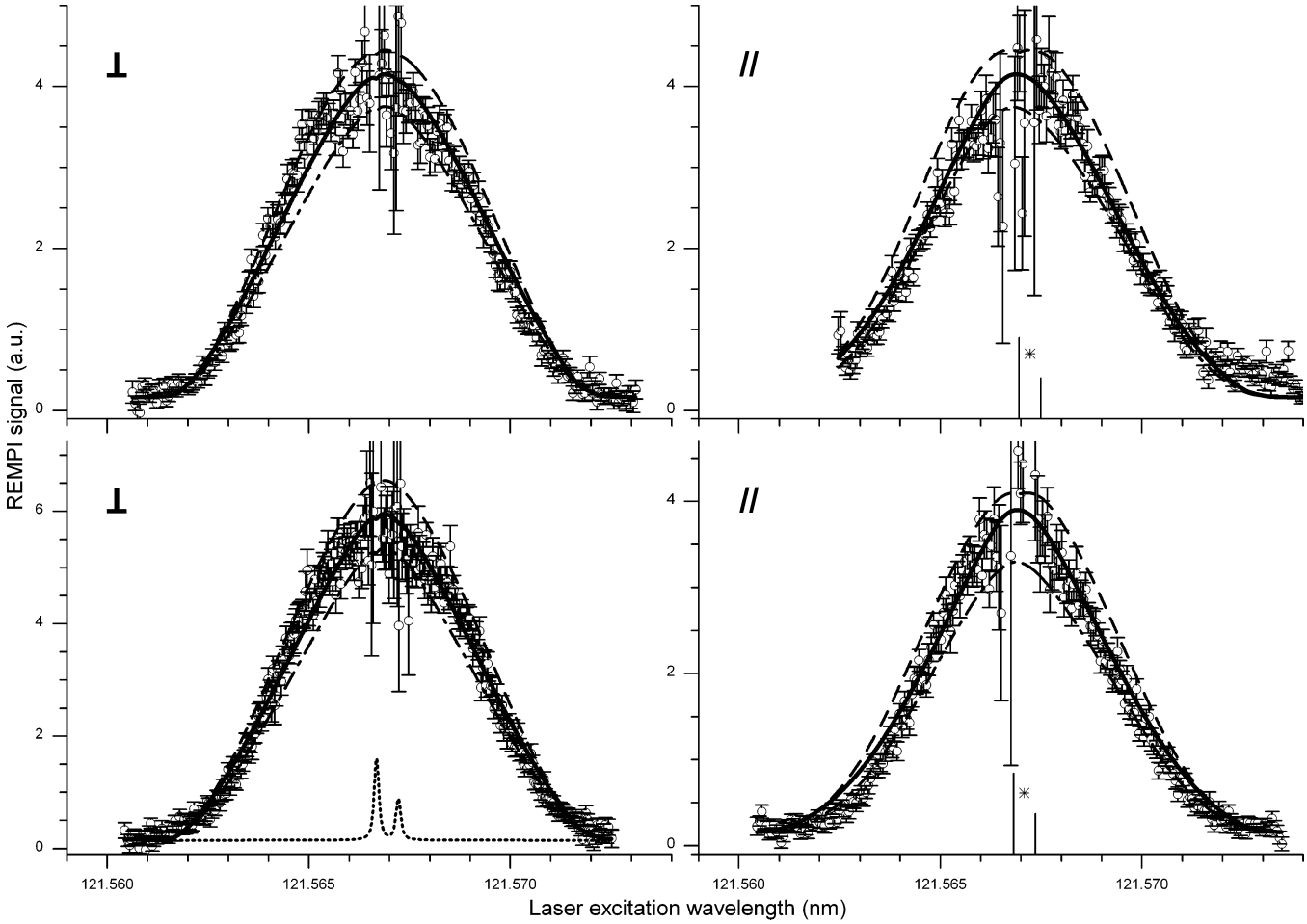

Figure 4. DF spectra of the H product from the C + H_2CCCH_2 reaction at 0.8 (lower row), 5.2 (upper row left), and 3.4 kJ mol^{-1} (upper row right) in the perpendicular (⊥) and parallel (//) configurations. Experimental (○); Fitting functions: best fit (solid line); dashed and dashed-dotted lines limit the range of acceptable fits; apparatus function (dotted line). Lyman-α ($^2S_{1/2} \rightarrow {}^2P^\circ_{3/2}$ and $^2S_{1/2} \rightarrow {}^2P^\circ_{1/2}$) line positions in the CM frame are indicated (*). Intensities are given in arbitrary units (a.u.).

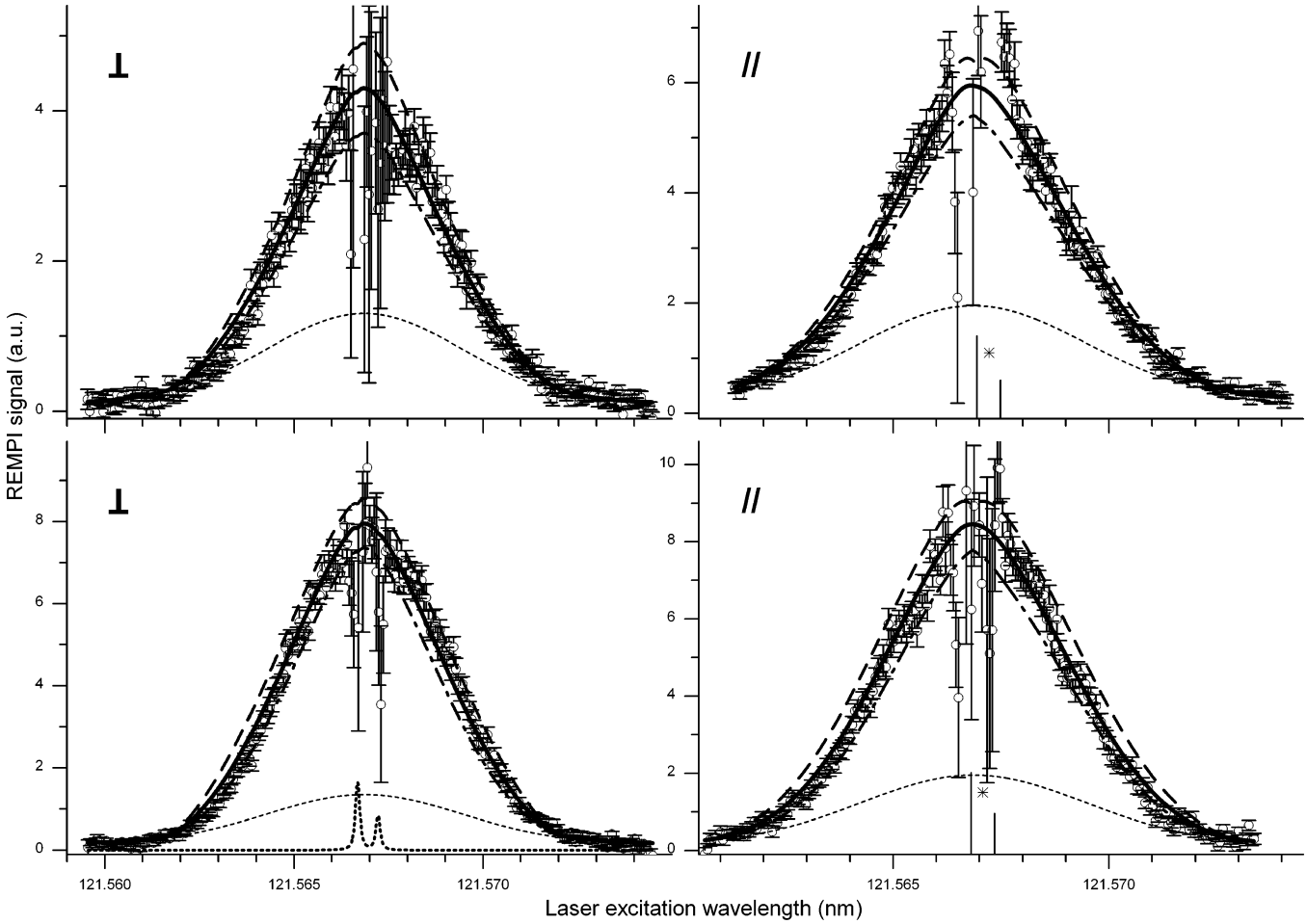

Figure 5. DF spectra of the H product from the C + H_3CCCH reaction at 0.8 (lower row) and 3.4 kJ mol^{-1} (upper row), in the perpendicular (⊥) and p*a*rallel (//) configurations. Experimental (○); Fitting functions: best fit (solid line); dashed and dashed-dotted lines limit the range of acceptable fits; H spurious signal due to photodissociation of H_3CCCH (short dashed line); apparatus function (dotted line). Lyman-α ($^2S_{1/2} \rightarrow {}^2P°_{3/2}$ and $^2S_{1/2} \rightarrow {}^2P°_{1/2}$) line positions in the CM frame are indicated (*). Intensities are given in arbitrary units (a.u.).

TABLE 4: Main Reaction Channels

	$\Delta_r H°_0$/kJ mol^{-1}		
C(^3P_J) + C_2H_4(X^1A_g) → $H_2CCCH(X^2B_2)$ + H($^2S_{1/2}$)	−190.0	*a*	(1)
C(^3P_J) + H_2CCCH_2(X^1A_1) → *i*-$H_2CCCCH(X^2A')$ + H($^2S_{1/2}$)	−189.6	*b*	(2)
C(^3P_J) + $H_3CCCH(X^1A_1)$ → *i*-$H_2CCCCH(X^2A')$ + H($^2S_{1/2}$)	−183.2	*b*	(3)

[a] From calculations by T. N. Le et al. (ref 24); a similar value, −191.4 kJ mol^{-1}, is derived from the enthalpy of the $^1CH_2$ + C_2H_2 → C_3H_3 + H reaction studied in a crossed beam experiment by Davis et al. (ref 25). [b] From tabulated values of formation enthalpies (in kilojoules per mole) at 0 K (ref 26) for C (711.2), H (216.0), allene (198.4), and methylacetylene (192.0), and $\Delta_f H°_0$(*i*-C_4H_3) = 504.0 from a crossed beam study of the reaction C_2 + C_2H_4 → C_4H_3 + H (ref 27).

4. Results and Discussion

The model has been applied to retrieve DCSs of the reactions of carbon atoms with ethylene, allene, and methylacetylene. The main reaction channels are listed in Table 4.

The laser excitation spectra observed in the present experiments are shown in Figures 3 (C + C_2H_4), 4 (C + H_2CCCH_2), and 5 (C + H_3CCCH). The scatter in the data of the experimental DF spectra in the vicinity of the line center is due to subtraction of background signal (ii) due to cold H atoms within the C-atom beam. The distribution functions used to fit the data are shown in Figures 6 and 7.

4.1. Reaction C(^3P_J) + C_2H_4(X^1A_g) → $H_2CCCH(X^2B_2)$ + H($^2S_{1/2}$). The dynamics of this reaction were described in a previous paper.[14] ICSs were recorded in Bordeaux between 0.49 and 24.9 kJ mol^{-1}, whereas DCSs were obtained in Perugia at energies from 9.1 to 30.8 kJ mol^{-1}; it thus provides a good test for our model.

The data could be fitted with a single reaction path, yielding H_2CCCH + H. Other much less exoergic paths, yielding H + *c*-C_3H_3 isomers or H_3CCC, were included in the Perugia fit, with branching ratios of 14, 5, and 2% for collision energies of 30.8, 17.2, and 9.1 kJ mol^{-1}, respectively. This was shown to be consistent with our ICS, which exhibited a sharp change in the slope at ca. 6 kJ mol^{-1} assigned to the onset of these less exoergic reaction channels. It is thus very likely that contributions of these channels are negligible at the lower energies sampled in the present experiments.

The following functions were used to fit our data. The recoil energy distribution function, given by eq 6 with $m = 0.6$, $n = 1.1$, and $p = 3.6$, is almost identical (on a reduced energy scale) to the Perugia one at 9.1 kJ mol^{-1}. (See Figure 6a.) This corresponds to a fraction of energy released in translation, f_T = 38%. At low energy (0.8 kJ mol^{-1}), a uniform angular distribution $T(\theta) = 1$ (Figure 7a) yielded the best fit to experimental spectra, whereas at higher energy (5.6 kJ mol^{-1}), the best fit was obtained with the same function as that in Perugia (at 9.1 kJ mol^{-1}), that is, with a slight dissymmetry of ca. −10% on the backward side (Figure 7b). This is consistent

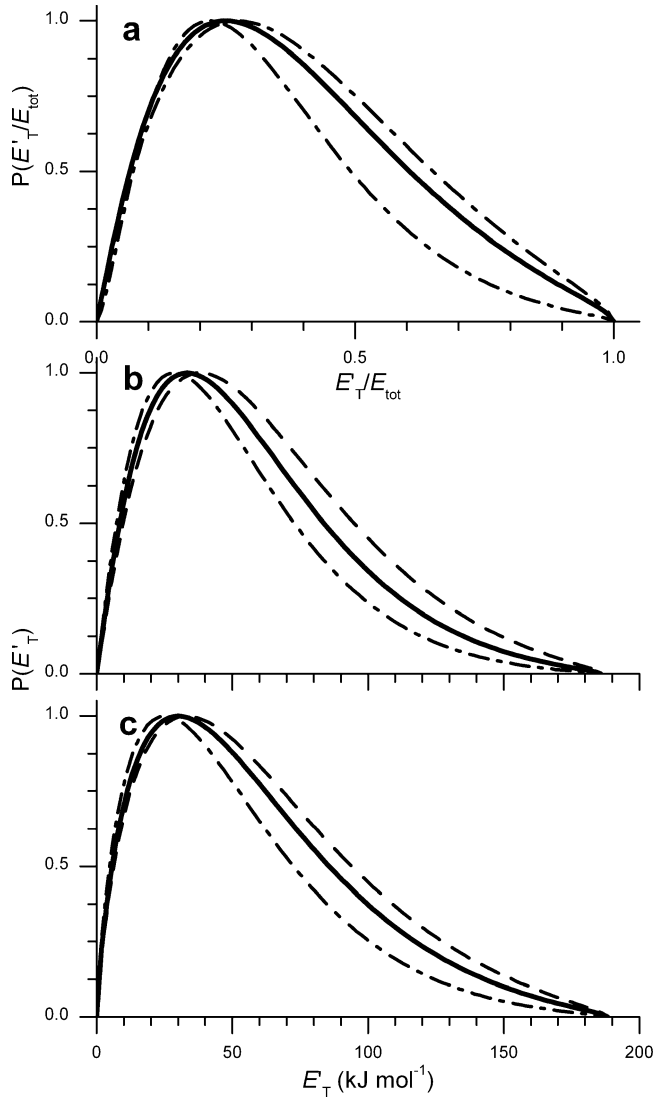

Figure 6. Recoil energy distribution functions used to fit DF spectra of the H-product from: (a) C + C_2H_4 and C + H_2CCCH_2 at any energy (note the reduced energy scale); (b) C + H_3CCCH at 0.8 kJ mol^{-1}, and (c) C + H_3CCCH at 3.3 kJ mol^{-1}. Best fit functions (solid line); dashed and dashed-dotted lines limit the range of acceptable fits.

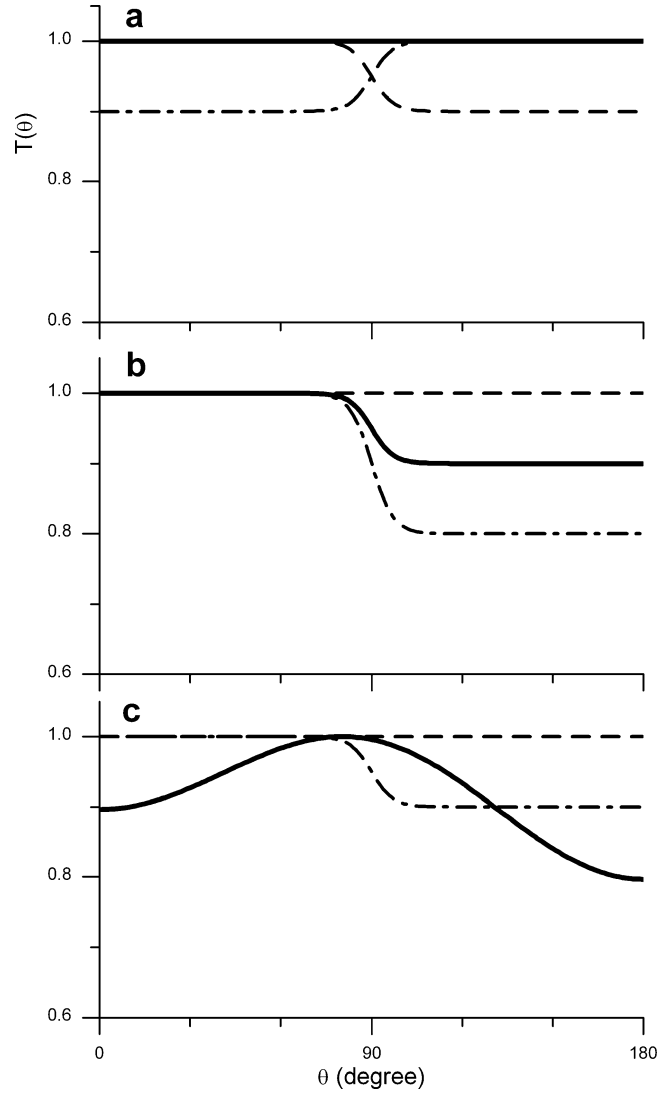

Figure 7. Angular distribution functions used to fit DF spectra of the H product from (a) C + C_2H_4 at 0.7 kJ mol^{-1} and C + H_3CCCH; (b) C + C_2H_4 at 5.6 kJ mol^{-1}; and (c) C + H_2CCCH_2. Best fit functions (solid line); dashed and dashed-dotted lines limit the range of acceptable fits.

with an indirect mechanism with a complex lifetime decreasing when increasing total energy, hence resulting in a dissymmetry in the angular distribution. The distributions yielding an acceptable fit but of lower quality are displayed in Figures 6 and 7 (dashed and dashed-dotted lines). The spectra were computed with a reaction energy: $\Delta_r H_0^\circ = -190$ kJ mol^{-1}, which is in good agreement with the value from Le et al.[24] but lower than the value $\Delta_r H_0^\circ = -215$ kJ mol^{-1} deduced in the CMB experiments of Kaiser et al.[28] at $E_T = 17.1$ and 38.3 kJ mol^{-1}.

The excellent agreement in the DCSs found in Perugia and Bordeaux with CMB experiments of very different concepts provides the validation of our model.

4.2. Reaction C(^3P_J) + H_2CCCH_2(X^1A_1) → *i*-H_2CCCCH(X^2A') + H($^2S_{1/2}$). This reaction has been studied by Kaiser et al.[29] at significantly higher collision energies (19.6 and 38.8 kJ mol^{-1}).

The DF spectra recorded at 0.8, 3.4, and 5.2 kJ mol^{-1} could be fitted again with a single contribution, with a reaction energy $\Delta_r H_0^\circ = -190$ kJ mol^{-1}, consistent with the H-elimination path yielding the *i*-C_4H_3 isomer (1-butene-3-yne-2-yl). The *n* isomers lie ca. 40 kJ mol^{-1} above. The same recoil energy distribution function as that for C + C_2H_4 (Figure 6a) was used at all energies (again with $f_T = 38\%$). However, a uniform angular distribution could not give a satisfying fit for spectra in parallel and perpendicular configurations at a given energy, the fitting function being too broad or too narrow in the parallel or perpendicular configurations, respectively. To reconcile both sets of data, we need to use a slightly equatorial distribution with a weak forward/backward dissymmetry, as shown in Figure 7c. The product recoil energy distributions are comparable to those used by Kaiser et al.,[29] although slightly warmer (maximum probability at $E'_T/E_{tot} = 25\%$ instead of 17−22%). The angular distribution, however, departs from the almost isotropic one found by these authors. In particular, the equatorial contribution might be due to complexes resulting from C-atom addition on one allenic bond and dissociating before having time to perform a complete rotation: this should indicate that reactive collisions, even at the very low collision energies sampled in the present work, could keep a relatively direct character.

4.3. Reaction C(^3P_J) + H_3CCCH(X^1A_1) → *i*-H_2CCCCH(X^2A') + H($^2S_{1/2}$). This reaction has also been studied by Kaiser et al.[30] at collision energies of 20.4 and 33.2 kJ mol^{-1}.

The DF spectra recorded at 0.8 and 3.4 kJ mol^{-1} could be fitted again with a single contribution with a reaction energy

$\Delta_r H_0^\circ = -185$ kJ mol^{-1}, which is consistent with the H-elimination path yielding the *i*-C_4H_3 isomer.

Similar recoil energy distribution functions as those for C + C_2H_4 were used, however these were slightly colder: $P(E'_T)$ from eq 6 with $m = 0.6$, $n = 1.1$, and $p = 5.4$, giving a maximum probability at $E'_T = 33$ kJ mol^{-1}, for $E_T = 0.8$ kJ mol^{-1} (Figure 6b), and $m = 0.6$, $n = 0.8$, and $p = 4.3$, giving a maximum probability at $E'_T = 30$ kJ mol^{-1}, for $E_T = 3.4$ kJ mol^{-1} (Figure 6c). Both distributions yield the same value of the fraction of energy released in translation, $f_T = 31\%$. The distributions both peak at almost the same energy as Kaiser's distributions (around 30−40 kJ mol^{-1}), but both extend up to the maximum available energy, in contrast with Kaiser's distribution at 20.4 kJ mol^{-1}; the latter does not extend beyond 110−170 kJ mol^{-1}, that is, 45−105 kJ mol^{-1} below the maximum energy available for the H + *i*-C_4H_3 path. A uniform angular distribution was used for both energies, as in ref 30 at 20.4 kJ mol^{-1}. These findings are consistent with the results of Kaiser et al.[30] at $E_T = 33.2$ kJ mol^{-1} but not with those at $E_T = 20.4$ kJ mol^{-1}, although the present data have been obtained at much lower energies. These authors, by comparison with the C + H_2CCCH_2 reaction, attributed this difference to a change in the dynamics of the C + H_3CCCH reaction at 20.4 kJ mol^{-1}, invoking the formation of distinct and less-stable C_4H_3 isomers. Despite the (modest) differences in the angular distributions, these two reactions are likely to proceed with very similar dynamics, yielding most probably the same products (*i*-$H_2CCCCH(X^2A')$ + $H(^2S_{1/2})$).

5. Conclusions

The dynamics of H-atom elimination reactions of C atoms with ethylene, allene, and methylacetylene, which are of interest for interstellar cloud chemistry, have been investigated in a CMB experiment with variable beam intersection angle and 1 + 1′ REMPI TOF MS detection of the H-atom product. The DCSs have been obtained at collision energies substantially lower ($E_T = 0.7$ to 0.8 kJ mol^{-1} compared with $E_T > 9$ kJ mol^{-1} (for C + C_2H_4) or 20 kJ mol^{-1} (for C + C_3H_4)) than previous CMB studies of the same reactions. The low collision energies attained in this study approach those that are prevalent in the coldest objects of the universe. Indeed, temperatures ranging from 10 K in cold, dark clouds to 100 K in translucent clouds correspond to mean kinetic energies of Maxwell distributions $\langle E_T \rangle = {}^3/_2\mathbf{R}T$ from 0.13 to 1.3 kJ mol^{-1}. The results can thus be truly considered to be relevant to interstellar cloud chemistry.

Acknowledgment. The support of this research by the Programme National Physique Chimie du Milieu Interstellaire and the Conseil Régional d'Aquitaine is gratefully acknowledged. This work is also supported by the European Union Marie-Curie Human Resources and Mobility Programme, including a postdoctoral fellowship for K.M.H. under contract MCRTN-CT-2004-512302, Molecular Universe.

Appendix: Conversion Flux-to-Density

The number of H atoms present in the detection volume at the probing time (defined as $t = 0$) is obtained by integrating the flux of production (given by eq 11) from $t = -\infty$ to 0. Indeed, when dealing with pulsed beams, no steady state can be reached (which should reduce the flux-to-density conversion to a simple division by v', provided that v' does not vanish!). A species produced at time $t \leq 0$ with a given {LAB} velocity $\mathbf{v}'$ in a volume element dV centered at point M(t) must be in the volume viewed by the detector (centered at the beam intersection point, O) to contribute to the signal. The resulting constraint reads: $\vec{MO} = v'\vec{t}$. Its contribution to the signal will depend on the reagent densities when it was formed. It is thus necessary to model these densities. As in a former study,[31] beams are modeled with a Gaussian radial profile (cylindrical symmetry around the axis of propagation) and also a Gaussian temporal profile (along the propagation axis)

$$n_i[\mathbf{M}(t)] = n_i^0 \exp\left\{-\frac{\rho_i^2}{\delta_i^2}\right\} \exp\left\{-\frac{\Delta t_i^2}{\tau_i^2}\right\} \tag{A1}$$

where for each beam i, n_i^0 stands for the maximum density, ρ_i stands for the distance from $\mathbf{M}(t)$ to the propagation axis, δ_i represents the half-width at 1/e of the Gaussian radial profile, $\Delta t_i = \Delta\xi(t)/v_i$ represents the time shift between $\mathbf{M}(t)$ and the maximum of the beam at time t, v_i is the {LAB} velocity, and τ_i is the half-width at 1/e of the Gaussian temporal profile; $\Delta\xi(t)$ stands for the distance between $\mathbf{M}$ projection on the beam axis and the position of the maximum.

If the probed volume ΔV is sufficiently small to consider the concentrations of both reagents to be homogeneous within ΔV, integration on dV is straightforward (replacing dV by ΔV)

$$\frac{d^3N}{d^2\omega\, dw'} = \int_{-\infty}^{0} \left\{\frac{d^3\dot{N}}{d^2\omega\, dw'}\right\} dt$$

$$= \frac{\sigma_R}{2\pi}\Delta V v_r \int_{-\infty}^{0} \{n_1[M(t)]n_2[M(t)]P(w')T(\theta)\}\, dt \tag{A2}$$

Let X_M, Y_M, and Z_M be the coordinates of $\mathbf{M}$

$$\begin{cases} X_M = \{v_X(G) + w'_X\}t = V_{X_M}t \\ Y_M = \{w'_Y\}t = V_{Y_M}t \\ Z_M = \{v_Z(G) + w'_Z\}t = V_{Z_M}t \end{cases} \tag{A3a}$$

with

$$\begin{cases} V_{X_M} = \{v_X(G) + w'_X\} \\ V_{Y_M} = \{w'_Y\} \\ V_{Z_M} = \{v_Z(G) + w'_Z\} \end{cases} \tag{A3b}$$

The position of M(t) relative to each beam is given in the following paragraphs.

For the coreactant beam: The beam propagates along an OZ′ axis with an angle $\gamma = \{OZ'-OZ\}$. Let $\{\mathbf{X}', \mathbf{Y}, \mathbf{Z}'\}$ be the frame obtained by rotation around the $\mathbf{Y}$ axis by an angle γ. In this frame, $\mathbf{X}'$ and $\mathbf{Y}$ are perpendicular to the propagation axis (giving the radial distance), whereas the longitudinal (temporal) profile lies along $\mathbf{Z}'$. In this frame, M coordinates become

$$\begin{cases} X'_M = X_M \cos\gamma - Z_M \sin\gamma \\ Y_M = \text{unchanged} \\ Z'_M = X_M \sin\gamma + Z_M \cos\gamma \end{cases} \tag{A4}$$

The distance to the axis $\mathbf{Z}'$ is simply

$$\rho_1^2 = \{X_M \cos\gamma - Z_M \sin\gamma\}^2 + Y_M^2$$
$$= [\{V_{X_M} \cos\gamma - V_{Z_M} \sin\gamma\}^2 + V_{Y_M}^2]t^2 \quad \text{(A5)}$$

whereas the shift to the maximum on $\mathbf{Z}'$ is $\Delta Z' = Z'_M - v_1 t$, resulting in a time shift

$$\Delta t = \Delta Z'/v_1 = Z'_M/v_1 - t = \frac{X_M \sin\gamma + Z_M \cos\gamma}{v_1} - t$$
$$= \frac{V_{X_M} \sin\gamma + V_{Z_M} \cos\gamma - v_1}{v_1} t \quad \text{(A6)}$$

It can thus be written that

$$n_1[M(t)] = n_1^0 \exp\{-\alpha_1^2 t^2\} \quad \text{(A7)}$$

with

$$\alpha_1^2 = \frac{\{V_{X_M} \cos\gamma - V_{Z_M} \sin\gamma\}^2 + V_{Y_M}^2}{\delta_1^2} + \frac{[V_{X_M} \sin\gamma + V_{Z_M} \cos\gamma - v_1]^2}{\tau_1^2 v_1^2} \quad \text{(A8)}$$

For the atom beam: Because the beam propagates along the $\mathbf{Z}$ axis, the distance to the beam axis is

$$\rho_2^2 = X_M^2 + Y_M^2 = \{V_{X_M}^2 + V_{Y_M}^2\}t^2 \quad \text{(A9)}$$

The shift to the maximum on $\mathbf{Z}$ is $\Delta Z = Z_M - v_2 t$, resulting in a time shift

$$\Delta t = \Delta Z/v_2 = \frac{V_{Z_M} - v_2}{v_2} t \quad \text{(A10)}$$

This becomes

$$n_2[M(t)] = n_2^0 \exp\{-\alpha_2^2 t^2\} \quad \text{(A11)}$$

where

$$\alpha_2^2 = \frac{V_{X_M}{}^2 + V_{Y_M}{}^2}{\delta_2^2} + \frac{[V_{Z_M} - v_2]^2}{\tau_2^2 v_2^2} \quad \text{(A12)}$$

Let's now integrate eq A2: because $P(w')$ and $T(\theta)$ do not depend on time, it now becomes

$$\int_{-\infty}^{0} \{n_1[M(t)]n_2[M(t)]P(w')T(\theta)\}\, dt = P(w')T(\theta) \int_{-\infty}^{0} \{n_1[M(t)]n_2[M(t)]\}\, dt \quad \text{(A13)}$$

Replacing the densities by the Gaussian function defined above gives

$$\int_{-\infty}^{0} \{n_1[M(t)]n_2[M(t)]\}\, dt = n_1^0 n_2^0 \times \int_{-\infty}^{0} \{\exp\{-[\alpha_1^2 + \alpha_2^2]t^2\}\}\, dt \quad \text{(A14)}$$

The right part is simply the integral of a Gaussian function

$$\int_{-\infty}^{0} \{n_1[M(t)]n_2[M(t)]\}\, dt = n_1^0 n_2^0 \frac{\sqrt{\pi}}{2} \frac{1}{\sqrt{\alpha_1^2 + \alpha_2^2}} \quad \text{(A15)}$$

which gives the final result

$$\frac{d^3N}{d^2\omega\, dw'} = n_1^0 n_2^0 \Delta V \frac{\sigma_R}{2\pi} v_r P(w') T(\theta) \frac{\sqrt{\pi}}{2} \frac{1}{\sqrt{\alpha_1^2 + \alpha_2^2}} \quad \text{(A16)}$$

Note that the term

$$\frac{1}{2\pi} \frac{\sqrt{\pi}}{2} \frac{1}{\sqrt{\alpha_1^2 + \alpha_2^2}} = \Delta t(w', \omega) \quad \text{(A17)}$$

corresponds to the time during which both reactant beams can interact to give the probed product (here H atoms) with a given {LAB} velocity vector. It thus depends on geometrical (beam dimensions, crossing angle, etc.) as well as kinematic (velocities, pulsed beam durations, etc.) factors.

The solid angle ω will be expressed as a function of (θ, φ) or (α, β) depending on the probe configuration.

Integrating eq A17 with respect to all possible orientations around the laser axis yields the following average interaction times, which are used in the calculation of the Doppler−Fizeau spectra

In the parallel configuration:

$$\langle \Delta t \rangle_\varphi = \frac{1}{4\sqrt{\pi}} \int_0^{2\pi} \frac{d\varphi}{\sqrt{\alpha_1^2 + \alpha_2^2}} \quad \text{(A18)}$$

In the perpendicular configuration:

$$\langle \Delta t(\alpha_j) \rangle_\beta = \frac{1}{4\sqrt{\pi}} \sum_i \frac{T(\theta[\alpha_j, \beta_i]}{\sqrt{\alpha_1^2 + \alpha_2^2}} \delta\beta \quad \text{(A19)}$$

Note that in the latter case $T(\theta)$ is included in the averaging over β because θ depends on β.

References and Notes

(1) (a) Bergmann, K.; Demtröder, W.; Hering, P. *Appl. Phys.* **1975**, *8*, 65. (b) Bergmann, K.; Hefter, U.; Hering, P. *J. Chem. Phys.* **1976**, *65*, 488.

(2) (a) Kinsey, J. L. *J. Chem. Phys.* **1977**, *66*, 2560. (b) Murphy, E. J.; Brophy, J. H.; Arnold, G. S.; Dimpfl, W. L.; Kinsey, J. L. *J. Chem. Phys.* **1979**, *70*, 5910. (c) Murphy, E. J.; Brophy, J. H.; Kinsey, J. L. *J. Chem. Phys.* **1981**, *74*, 331. (d) Serri, J. A.; Kinsey, J. L.; Pritchard, D. E. *J. Chem. Phys.* **1981**, *75*, 663.

(3) Billy, N.; Girard, B.; Gouédard, G.; Vigué, J. *Laser Chem.* **1990**, *10*, 319.

(4) (a) L'Hermite, J.-M.; Rahmat, G.; Vetter, R. *J. Chem. Phys.* **1990**, *93*, 434. (b) L'Hermite, J.-M.; Rahmat, G.; Vetter, R. *J. Chem. Phys.* **1991**, *95*, 3347.

(5) Che, D.-C.; Liu, K. *Chem. Phys.* **1996**, *207*, 367.

(6) Schnieder, L.; Seekamprahn, K.; Liedeker, F.; Steuwe, H.; Welge, K. H. *Faraday Discuss.* **1991**, *91*, 259–269.

(7) Dong, F.; Lee, S.-H.; Liu, K. *J. Chem. Phys.* **2000**, *113*, 3633.

(8) Qiu, M.; Ren, Z.; Che, L.; Dai, D.; Harich, S. A.; Wang, X.; Yang, X.; Xu, C.; Xie, D.; Gustafsson, M.; Skodje, R. T.; Sun, Z.; Zhang, D. H. *Science* **2006**, *311*, 1440.

(9) Dong, F.; Lee, S.-H.; Liu, K. *J. Chem. Phys.* **2001**, *115*, 1197.

(10) Wang, X.; Dong, W.; Xiao, C.; Che, L.; Ren, Z.; Dai, D.; Wang, X.; Casavecchia, P.; Yang, X.; Jiang, B.; Xie, D.; Sun, Z.; Lee, S.-Y.; Zhang, D. H.; Werner, H.-J.; Alexander, M. H. *Science* **2008**, *322*, 573.

(11) (a) Hsu, Y.-T.; Liu, K. *J. Chem. Phys.* **1997**, *107*, 1664. (b) Lee, S.-H.; Liu, K. *J. Chem. Phys.* **1999**, *111*, 4351.

(12) Aoiz, F. J.; Bañares, L.; Castillo, J. F.; Herrero, V. J.; Martinez-Haya, B.; Honvault, P.; Launay, J. M.; Liu, X.; Lin, J. J.; Harich, S. A.; Wang, C. C.; Yang, X. *J. Chem. Phys.* **2002**, *116*, 10692.

(13) Costes, M.; Daugey, N.; Naulin, C.; Bergeat, A.; Leonori, F.; Segolini, E.; Petrucci, R.; Balucani, N.; Casavecchia, P. *Faraday Discuss.* **2006**, *133*, 157.

(14) Geppert, W. D.; Naulin, C.; Costes, M.; Capozza, G.; Cartechini, L.; Casavecchia, P.; Volpi, G. G. *J. Chem. Phys.* **2003**, *119*, 10607.

(15) Chastaing, D.; Le Picard, S. D.; Sims, I. R.; Smith, I. W. M. *Astron. Astrophys.* **2001**, *365*, 241.

(16) Chastaing, D.; Le Picard, S. D.; Sims, I. R.; Smith, I. W. M.; Geppert, W. D.; Naulin, C.; Costes, M. *Chem. Phys. Lett.* **2000**, *331*, 170.

(17) Naulin, C.; Costes, M. *Chem. Phys. Lett.* **1999**, *310*, 231.

(18) Gentry, W. R. In *Atomic and Molecular Beam Methods*; Scoles, G., Ed.; Oxford University Press: New York, 1988; Vol. 1, p 54.

(19) Dyer, P. E.; Snelling, H. V.; Walton, C. D. *Meas. Sci. Technol.* **2002**, *13*, 92.

(20) Wiley, W. C.; McLaren, I. H. *Rev. Sci. Instrum.* **1955**, *26*, 1150.

(21) (a) Bonnet, L.; Rayez, J.-C.; Casavecchia, P. *Phys. Chem. Chem. Phys.* **2000**, *2*, 741. (b) See also: Bergeat, A.; Cartechini, L.; Balucani, N.; Capozza, G.; Phillips, L. F.; Casavecchia, P.; Volpi, G. G.; Bonnet, L.; Rayez, J.-C. *Chem. Phys. Lett.* **2000**, *327*, 197.

(22) Levine R. D. Bernstein R. B. *Molecular Reaction Dynamics and Chemical Reactivity*; Oxford University Press: New York, 1987; pp 260−276.

(23) The CM velocity vector is opposite to the laser axis, *L*. Its projection on *L* is thus negative ($-w_C$).

(24) Le, T. N.; Lee, H. Y.; Mebel, A. M.; Kaiser, R. I. *J. Phys. Chem. A* **2001**, *105*, 1847.

(25) Davis, H. F.; Shu, J.; Peterka, D. S.; Ahmed, M. *J. Chem. Phys.* **2004**, *121*, 6254.

(26) (a) Cox, J. D. Wagman, D. D. Medvedev, V. A. *CODATA Key Values for Thermodynamics*; Hemisphere: New York, 1989. (b) Gurvich, L. V. Veyts, I. V. Alcock, C. B. *Thermodynamic Properties of Individual Substances*, 4th ed.; Hemisphere: New York, 1989.

(27) Gu, X.; Guo, Y.; Zhang, F.; Mebel, A. M.; Kaiser, R. I. *Chem. Phys.* **2007**, *335*, 95.

(28) Kaiser, R. I.; Lee, Y. T.; Suits, A. G. *J. Chem. Phys.* **1996**, *105*, 8705.

(29) Kaiser, R. I.; Mebel, A. M.; Chang, A. H. H.; Lin, S. H.; Lee, Y. T. *J. Chem. Phys.* **1999**, *110*, 10330.

(30) Kaiser, R. I.; Stranges, D.; Lee, Y. T.; Suits, A. G. *J. Chem. Phys.* **1996**, *105*, 8721.

(31) Naulin, C.; Costes, M.; Benseddik, A.; Dorthe, G. *Laser Chem.* **1988**, *8*, 283.

JP9038545